1 **Revision 2**

2   Word Count: 7100

3 **Magnesio-ferri-hornblende, □Ca$_2$(Mg$_4$Fe^{3+})[(Si$_7$Al)O$_{22}$](OH)$_2$, a new member of**

4 **the amphibole supergroup**

5 Yongmei Zhang[1,2], Xuexiang Gu[1,2*], Ting Li[3], Guang Fan[3], Yingshuai Zhang[2],

6 Tao Wang[2], and Jialin Wang[1]

7 [1]State Key Laboratory of Geological Processes and Mineral Resources, China

8   University of Geosciences, Beijing 100083, China

9 [2]School of Earth Sciences and Resources, China University of Geosciences, Beijing

10   100083, China

11 [3]Beijing Research Institute of Uranium Geology, Beijing 100029, China

12 *E-mail: xuexiang_gu@163.com

13 **ABSTRACT**

14   Magnesio-ferri-hornblende, ideally □Ca$_2$(Mg$_4$Fe^{3+})[(Si$_7$Al)O$_{22}$](OH)$_2$, is a new

15 mineral of the amphibole supergroup from the Husite granitic complex related to

16 skarn-type Fe-Cu mineralization in the Western Tianshan, Xinjiang, northwestern

17 China. The new species and the new name have been approved by the IMA-CNMNC

18 (2021-100). Magnesio-ferri-hornblende is dark green to green-black with a vitreous

19 lustre and a pale gray-green to gray-white streak. It occurs mostly as subhedral-

20 columnar crystals with a length of 0.5 to 3 mm and shows well-developed {110}

21   cleavage. It has a Mohs hardness of ~5 and a Vickers microhardness of 389-448

22   kg/mm^2 (VHN load in 100g) and is brittle with a conchoidal fracture. The measured

23   and calculated densities are 3.275(6) and 3.204 g/cm^3, respectively. In transmitted

24   plane-polarized light, magnesio-ferri-hornblende is strongly pleochroic, X = pale

25   yellow, Y = yellowish brown, Z = dark yellowish green. It is biaxial (−), α = 1.651(2),

26   β = 1.658(2), γ = 1.662(2), $2V$ (meas.) = 73 (1)º to 82 (1)º and $2V$ (calc.) = 73.9 (1)º,

27   dispersion is $r > v$, medium to strong. The orientation is: $Y // b$, $X^\wedge a$=31.5º (β obtuse),

28    $Z^\wedge c$=16.5 º (β acute).

29   Magnesio-ferri-hornblende is monoclinic, space group $C2/m$, a = 9.8620(3), b =

30   18.1060(5), c = 5.30810(10) Å, β = 104.8480(10)º, V = 916.17(4) Å^3, Z = 2. The

31   strongest seven lines in the powder X-ray diffraction pattern are [d in Å(I)(hkl)]:

32   8.397(52)(110), 3.383(41)(150), 2.717(100)(151), 2.597(84)(061), 2.545(61)(20$\overline{2}$),

33   1.854(49)(1$\overline{7}$$\overline{2}$), and 1.519(62)(6$\overline{2}$$\overline{2}$). Analysis by a combination of electron

34   microprobe and Mössbauer spectroscopy gave SiO_2 47.37, TiO_2 1.51, Al_2O_3 7.07,

35   Fe_2O_3 3.86, FeO 11.62, MgO 12.77, CaO 11.22, SrO 0.15, MnO 0.39, Na_2O 1.54,

36   K_2O 0.78, Cl 0.15, F 0, H_2O_{calc} 2.01, Cl≡O −0.03, sum 100.41 wt%. The empirical

37   formula calculated on the basis of 24 (O + OH + F + Cl) with (OH + F + Cl) = 2 apfu

38   is

39    $^A(\square_{0.62}Na_{0.23}K_{0.15})_{\Sigma1.00}$$^B(Ca_{1.76}Na_{0.21}Mn_{0.02}Sr_{0.01})_{\Sigma2.00}$$^C(Mg_{2.79}Fe^{2+}_{1.42}Fe^{3+}_{0.43}Ti_{0.17}Al_{0.16}$

40    $Mn_{0.03})_{\Sigma5.00}$$^T(Si_{6.94}Al_{1.06})_{\Sigma8.00}O_{22}$$^W(OH_{1.96}Cl_{0.04})_{\Sigma2.00}$. The crystal structure of magnesio-

41   ferri-hornblende was refined to an R_1 of 3.95% using 2185 data (>2σ) collected with

42   MoKa X-radiation. The A site is dominantly occupied by $\square$ where ^{A}(Na + K + 2Ca) ≤

43   0.5. ^{T}Al is ordered at the $T(1)$ site. $M(1)$ and $M(3)$ are dominantly occupied by Mg^{2+},

44   and $M(2)$ is occupied by both Mg^{2+} and high-charged cations. The new mineral occurs

45   most commonly in the porphyry-skarn Fe-Cu-Mo-Au- and hydrothermal Au-

46   mineralized granitoids with high oxygen fugacity, but is rare or absent in barren

47   intrusions. Its finding has important significance for magma fertility discrimination

48   and can potentially be used in regional exploration for porphyry-skarn ore system.

49   **KEY WORDS:** magnesio-ferri-hornblende, new amphibole, optical properties, electron-

50   microprobe analysis, crystal-structure refinement, magma fertility, Western Tianshan,

51   China.

52   **INTRODUCTION**

53   Amphiboles are common rock-forming minerals in a wide variety of rocks. The

54   amphibole supergroup minerals are prevalent in igneous and metamorphic rocks

55   formed under a broad temperature and pressure span, thus have a variety of chemical

56   compositions (Leake, 1997; Hawthorne et al., 2007, 2012). Amphiboles are useful in

57   understanding petrogenetic conditions and process, e.g., the Al-in-hornblende

58   geobarometer was consistently explored since 1980s (Hammarstrom and Zen, 1986;

59   Mutch et al., 2016 and references therein), and a series of amphibole

60   thermobarometric formulations can give precious information (P, T, fO_2, H_2O_{melt}) on

61   magmatic plumbing systems (Ridolfi et al., 2010; Ridolfi and Renzulli, 2012). The

62   general chemical formula of the amphibole supergroup can be written as

63    $AB_2C_5T_8O_{22}W_2$, where A = □, Na, K, Ca, Pb, Li; B = Na, Ca, Mn^{2+}, Fe^{2+}, Mg, Li; C =

64   Mg, Fe^{2+}, Mn^{2+}, Al, Fe^{3+}, Mn^{3+}, Cr^{3+}, Ti^{4+}, Li; T = Si, Al, Ti^{4+}, Be; W = (OH), F, Cl,

3

65   O^{2-}. According to the current amphibole nomenclature scheme proposed by

66   Hawthorne et al. (2012), the supergroup is divided into two groups of ^{W}(OH, F, Cl)-

67   dominant amphiboles and ^{W}O-dominant amphiboles (oxo-amphiboles). The new

68   mineral "magnesio-ferri-hornblende" reported in this study belongs to the calcium

69   amphibole subgroup of the ^{W}(OH, F, Cl)-dominant group.

70   In this contribution, the discovered amphibole has now been characterized as a new

71   mineral species named magnesio-ferri-hornblende, where the prefix "magnesio-"

72   indicates Mg dominance over C^{2+} cations and the prefix "ferri-" means Fe^{3+} is

73   dominant over C^{3+} cations. The new species and the new name have been approved by

74   the International Mineralogical Association Commission on New Minerals,

75   Nomenclature and Classification (IMA-CNMNC, 2021-100). Holotype material is

76   deposited in the Geological Museum of China, No. 16, Yangrou Hutong, Xisi, Beijing

77   100031, People's Republic of China, with the catalogue number M16131 (Zhang et al.,

78   2022). Significantly, magnesio-ferri-hornblende occurs most commonly in fertilized

79   felsic igneous rocks associated with porphyry-skarn Fe-Cu-Mo-Au mineralization, but

80   is far less common or absent in barren intrusions. Therefore, it could be served as a

81   potential mineral indicator for identifying fertile magmatic systems from barren felsic

82   igneous rocks.

83   **OCCURRENCE**

84   The new mineral magnesio-ferri-hornblende was firstly found in the Late

85   Devonian Husite granitic complex in the Boluokenu island arc belt of the Western

86   Tianshan, Xinjiang, NW-China (82°43'26" E, 44°5'25" N). Situated in the western

4

87   section of the Central Asia Orogenic Belt (Fig. 1a), the Boluokenu island arc belt is

88   one of the important metallogenic belts in the Western Tianshan, with a number of

89   skarn and porphyry Fe-Cu-Mo polymetallic deposits associated with granitoids that

90   formed during the Devonian to Early Carboniferous (Fig. 1b-c; Gu et al., 2014; Zhang

91   et al., 2016; Wang et al., 2018). Since its initial discovery in the Husite granitic

92   complex that is related to the Kekesala and Aimusidaiyi Fe-Cu skarn deposits,

93   magnesio-ferri-hornblende has been subsequently found in several other intrusions in

94   the belt, such as the Dawabulake granodiorite associated with the skarn-type Halegati

95   Fe-Cu and Muzuke Pb-Zn deposits, the porphyry Mo ore-related Lailisigaoer

96   plagiogranite porphyry, and the Nailenggele monzogranite (Fig. 1c).

97   The Husite intrusion elongates in NW direction, covering about 170 km^2 and

98   intruding into the Ordovician limestone (Fig. 1c). It is composed of monzonitic

99   granite, granodiorite, syenogranite, granitic aplite, dioritic porphyrite, gabbro and

100   mafic microgranular enclaves (MMEs). Magnesio-ferri-hornblende dominantly occurs

101   as subhedral-columnar crystals in the medium- to course-grained granodiorite

102   lithofacies (Fig. 2). The grain size ranges from 0.5 to 3 mm, and the aggregate size

103   varies from 0.5 to 1 cm. It is closely associated with plagioclase, quartz, K-feldspar,

104   biotite, magnesio-hastingsite, as well as small amounts of zircon, magnetite, apatite,

105   and sphene.

106 <center>**MINERAL CHARACTERIZATION**</center>

107 **Physical and optical properties**

108   Magnesio-ferri-hornblende is dark green to green-black with a vitreous luster. It has

109 a pale gray-green to gray-white streak and shows no fluorescence under long- or

110 short-wave ultraviolet light. It is brittle and shows a conchoidal fracture. The Vickers

111 microhardness is measured to be 389-448 kg/mm^2 (VHN load in 100g), and the

112 converted Mohs hardness is ~5. It has the characteristic perfect {110} cleavage of

113 amphiboles, intersecting at ~56°. The measured density is 3.275(6) g/cm^3 by

114 hydrostatic weighing method using the ALFA MIRAGE SD-200L electronic density

115 balance. The calculated density according to the empirical formula and unit cell

116 volume refined from single crystal X-ray diffraction (XRD) data is 3.204 g/cm^3.

117   In transmitted plane-polarized white light, magnesio-ferri-hornblende has strong

118 pleochroism, with X = pale yellow, Y = yellowish brown, and Z = dark yellowish

119 green. The orientation is $Y // b$, $X \wedge a$=31.5º, and $Z \wedge c$=16.5 º. Magnesio-ferri-

120 hornblende is biaxial negative, with indices of refraction α = 1.651 (2), β = 1.658 (2),

121 γ = 1.662 (2); $2V$ (meas.) = 73 (1)º to 82 (1)º and $2V$ (calc.) = 73.9 (1)º, under white

122 light. Dispersion is medium to strong, $r > v$. Gladstone-Dale parameters yielded a

123 compatibility index $(1-K_P/K_C)$ of 0.024, which is considered to be excellent

124 (Mandarino, 1981).

125 **Mössbauer, infrared and Raman spectroscopy**

126   The Mössbauer spectrum of magnesio-ferri-hornblende was measured using a

<center>6</center>

127   constant acceleration in transmission mode (Wissel MVT-1000) with a ^{57}Co/Rh

128   source at room temperature (20°C). The velocity was calibrated by 25 μm α-Fe foil

129   and the isomer shift relative to the center of α-Fe at room temperature. The Mössbauer

130   parameters are listed in Table 1, and the Mössbauer spectrum of the mineral is shown

131   in Fig. 3.

132   The infrared spectrum of magnesio-ferri-hornblende powder pressed in a KBr pellet

133   was analysed with a Perkin-Elemer Fourier transform infrared spectroscopy (FT-IR)

134   in the 400-4000 cm^{-1} wavelength range at a resolution of 4 cm^{-1} upon 16 scanning. A

135   pure KBr pellet was used as the reference sample. In the infrared spectrum of

136   magnesio-ferri-hornblende (Fig. 4), Si-O stretching vibrations are identified by two

137   absorption regions with bands at 1092 cm^{-1}, 1044 cm^{-1}, 987 cm^{-1}, and 951 cm^{-1}, and at

138   753 cm^{-1}, 688cm^{-1}, 660 cm^{-1}, and 603 cm^{-1}, respectively. In the low frequency range

139   between 600 cm^{-1} and 400 cm^{-1}, the bands at 508 cm^{-1} and 460 cm^{-1} should be

140   attributed to Si-O bending vibration and M-O vibration, respectively. The high-energy

141   OH stretching vibrations exhibit bands for the OH groups coordinated by cationic

142   triads: (MgMgMg/MgMgFe^{2+}–OH–A, 3688 cm^{-1}), (MgMgMg–OH–□, 3672 cm^{-1}),

143   and (MgFe^{2+}Fe^{2+}–OH–□, 3645 cm^{-1}). The bands were assigned in accordance with

144   Chukanov and Chervonnyi (2016), which further proved that the new mineral is Mg

145   and Fe^{2+} at the M(1, 3) sites in composition. The bands at 3434 cm^{-1} and 1632 cm^{-1} of

146   H$_2$O appear in both sample KBr pellet and pure KBr pellet with similar absorbance

147   extent, indicating that the H$_2$O comes from environments due to the hygroscopicity of

148   KBr under current experimental conditions.

149 Raman spectra of magnesio-ferri-hornblende were obtained using a Renishaw

150 Invia Reflex-type confocal Laser Raman microspectrometry with a laser excitation

151 wavelength of 514.5 nm (20 mW, 1μm). The most distinct Raman peak detected in the

152 magnesio-ferri-hornblende is around 666-725 cm^{-1} (Fig. 5), which is assigned to the

153 symmetric stretching vibrations of the Si-O-Si bridges (Apopei and Buzgar, 2010).

154 The OH stretching region is found in the spectral domain of 3644 cm^{-1}, 3659 cm^{-1} and

155 3673 cm^{-1}, consistent with other amphiboles studied by various authors (e.g., Huang,

156 2003; Su et al., 2009). The spectral bands around 532 cm^{-1} were assigned to the OH^-

157 group (OH^- translation, Kloprogge et al., 2001). The bands between 200 cm^{-1} to 300

158 cm^{-1} may be assigned to lattice vibration (Huang, 2003) and the O-H-O group

159 (Rinaudo et al., 2004).

160 **Chemical composition**

161 Magnesio-ferri-hornblende was analyzed by electron microprobe JXA-8100

162 operating in wavelength-dispersive mode with acceleration voltage 20 kV, beam

163 current 20 nA, and beam diameter 2 μm. The following standards and crystals were

164 used for $K\alpha$ X-ray lines: Si, Na: albite, Ti: rutile; Al: sanidine; Fe: hematite; Mg, Ca:

165 diopside; Sr: celestite; Mn: pyrophanite; K: biotite; Cl: tugtupite; OH: fluorapatite.

166 The average of 18 analyses on three crystals, under consideration of the Mössbauer

167 results, is given in Table 2.

168 The empirical chemical formula, calculated on the basis of 24 (O+OH+F) with

169 OH+F+Cl   =   2   apfu   is

170 $^A(\square_{0.62}Na_{0.23}K_{0.15})_{\Sigma 1.00}{}^B(Ca_{1.76}Na_{0.21}Mn_{0.02}Sr_{0.01})_{\Sigma 2.00}{}^C(Mg_{2.79}Fe^{2+}{}_{1.42}Fe^{3+}{}_{0.43}Ti_{0.17}Al_{0.16}$

171     $Mn_{0.03})_{\Sigma 5.00}{}^{T}(Si_{6.94}Al_{1.06})_{\Sigma 8.00}O_{22}{}^{W}(OH_{1.96}Cl_{0.04})_{\Sigma 2.00}$.   The   ideal   formula   is

172     $\square Ca_2(Mg_4Fe^{3+})(Si_7Al)O_{22}(OH)_2$, which requires SiO_2 49.90, Al_2O_3 6.05, CaO 13.31,

173   MgO 19.13, Fe_2O_3 9.47, H_2O 2.14, total 100 wt%.

174   **X-ray diffraction and structure refinement**

175   X-ray powder diffraction data were collected with a two-dimensional PHOTON

176   100 CMOS detector with Bruker D8 QUEST, using monochromated Mo$K\alpha$ radiation

177   (0.71073 Å) from a sealed microfocus tube. Generator settings were 50 kV and 1 mA.

178   The recorded pattern is reported in Table 3. The strongest seven diffraction lines are

179   [d in Å(I)(hkl)]: 8.397(52)(110), 3.383(41)(150), 2.717(100)(151), 2.597(84)(061),

180   2.545(61)($20\bar{2}$), 1.854(49)($1\bar{7}\bar{2}$), and 1.519(62)($6\bar{2}\bar{2}$). The unit-cell parameters refined

181   from the powder-XRD data (space group $C2/m$) are: a = 9.889 (5) Å; b =18.153 (6) Å;

182   c =5.313 (3) Å; β = 104.57 (3)°; V = 923.1 (7) Å^3; Z =2. The a:b:c ratio calculated

183   from unit-cell parameters is 0.5447 : 1 : 0.2932.

184   A crystal of 0.058×0.078×0.110 mm size was examined for the single crystal XRD

185   experiment, using a Bruker D8 QUEST diffractometer (IµS Tube, 100W, Mo$K\alpha$ λ =

186   0.71073 Å) and a PHOTON 100 CMOS detector. The frames were integrated with the

187   Bruker SAINT Software Package using a narrow-frame algorithm. The integration of

188   the data using a monoclinic unit cell yielded a total of 26665 reflections to a

189   maximum θ angle of 40.25° (0.55 Å resolution), of which 2953 were independent

190   (average redundancy 9.030, completeness = 100.0%, R_{int} = 7.26%, R_{sig} = 3.51%) and

191   2185 (73.99%) were greater than 2σ (F^2). The final cell constants of a = 9.8620(3) Å,

192   b = 18.1060(5) Å, c = 5.30810(10) Å, β = 104.8480(10)°, and V = 916.17(4) Å^3 are

193   based upon the refinement of the *XYZ*-centroids of 242 reflections above 20 $\sigma(I)$ with

194    $4.485° < 2\theta < 45.66°$. Data were corrected for absorption effects using the Multi-Scan

195   method (SADABS). The ratio of minimum to maximum apparent transmission was

196   0.918. Data collection information and structure-refinement parameters for magnesio-

197   ferri-hornblende are given in Appendix Table 1.

198   The structure was solved and refined using the Bruker SHELXTL Software

199   Package, using the space group $C2/m$, with $Z = 2$ yielding the formula unit,

200    $K_{0.07}Na_{0.72}Ca_{1.82}Mg_{3.06}Fe_{1.94}Si_{6.94}Al_{1.06}O_{24}Cl_{0.11}$. The final anisotropic full-matrix

201   least-squares free refinement on F^2 with 116 variables converged at $R_1 = 0.0395$ and

202    $wR_2 = 0.0775$ using 2185 data (>2σ). The goodness-of-fit was 1.058. On the basis of

203   the final model, the calculated density was 3.213 g/cm^3 and F(000), 875 e$^-$. Atom

204   coordinates, site occupancy factors and site-scattering factors, and anisotropic atomic

205   displacement parameters are given in Appendix Table 2, and selected interatomic

206   distances are listed in Table 4. Refined site-scattering values are given in Table 5. The

207   Crystallographic Information File (CIF) is available as Supplemental Material.

208   **Derivation of site populations**

209   The occupancy of A(m) and A(2) was fixed based on the EPMA results. There are no

210   restraints in B, M(1)$, M(2)and M(3) sites during structure refinement. The results of

211   structure refinement clearly show that A site is dominantly occupied by vacant, M(1)

212   and M(3) are dominantly occupied by Mg^{2+}, and M(2) is occupied by both Mg^{2+} and

213   high-charged cations.

214   Site populations were obtained considering the experimental mean bond lengths

10

215 and site-scattering values for the individual sites (Hawthorne et al., 1995; Oberti et al.,

216 2007). ^{T}Al is ordered at the $T(1)$ site, the occupancy of $^{T(1)}$Al is following the

217 equations $^{T(1)}$Al (apfu) = [<$T(1)$–O> − 1.6193] × 34.2199, and <$T(1)$–O> is 1.650 Å.

218 We get $^{T(1)}$Al (apfu) = 1.061 (Oberti et al., 2007). It is in excellent agreement with the

219 chemical analyses. So we fix the occupancy of Si (0.735) and Al (0.265) at $T(1)$ site.

220 The refined values of site-scattering obtained by structure refinement are in good

221 agreement with those calculated based on the proposed site populations (Hawthorne et

222 al., 1995). Calculation of the site populations (Table 5) was based on the <cat–O>

223 values of Mg: 2.078 Å, Al: 1.929 Å, Ti: 1.960 Å, Mn^{2+}: 2.173 Å, Fe^{2+}: 2.125 Å, and

224 Fe^{3+}: 2.025 Å (Oberti et al., 2016b).

225   **RELATION TO OTHER SPECIES**

226   The name "magnesio-ferri-hornblendite" has been used in the literature

227 (Zarubina et al., 2016), with no previous approval by the IMA-CNMNC. A certain

228 amount of hornblende EPMA data published in literatures should belong to magnesio-

229 ferri-hornblende, but the authors did not fully identify it and named it magnesio-

230 hornblende (e.g., He et al., 2018; Gong et al., 2018; and references in Appendix Table

231 3). Before the approval of magnesio-ferri-hornblende, there were four mineral species

232 approved by the IMA-CNMNC with hornblende root name, e.g., magnesio-

233 hornblende, ferro-hornblende, magnesio-ferri-fluoro-hornblende, and ferro-ferri-

234 hornblende. The differences between magnesio-ferri-hornblende and the known

235 species with hornblende root name are shown in Table 6.

236   According to "the IMA-CNMNC dominant-constituent rule revisited and

11

237   extended" (Hatert and Burke, 2008; Nickel and Grice, 1998) and "Nomenclature of

238   the amphibole supergroup" (Hawthorne et al., 2012), magnesio-ferri-hornblende

239   should be regarded as a new member of calcium amphibole subgroup. Magnesio-ferri-

240   hornblende is the Fe^{3+} dominant at C^{3+} analogue of magnesio-hornblende.

241   DISCUSSION

242   **Potential mineral indicator of fertile porphyry systems**

243   Recalculating the published amphibole data according to Hawthorne et al. (2012),

244   preliminary statistics show that magnesio-ferri-hornblende is distributed in various

245   types of rocks from more than 40 locations worldwide (Ghent et al., 1990; El-Shazly

246   et al., 1997; Mogessie et al., 2000; Zarubina et al., 2016; Horváth et al., 2019;

247   Stepanov et al., 2021; Gil et al., 2022; and references in Appendix Table 3).

248   Magnesio-ferri-hornblende occurs either in metamorphic rocks such as blueshist

249   (Ghent et al., 1990), epidote amphibolite (El-Shazly et al., 1997), dolomite (Zarubina

250   et al., 2016), and amphibolitized eclogite (Gil et al., 2022), or in mafic-ultramafic

251   igneous rocks (Liu et al., 2012; Mogessie et al., 2000; Zhang et al., 2021) and more

252   broadly in intermediate-acid intrusive rocks (for references see Appendix Table 3). Of

253   particular note is that the occurrence frequency of magnesio-ferri-hornblende in

254   fertilized felsic intrusions related to porphyry-skarn type Fe-Cu-Mo-Au polymetallic

255   and magmatic hydrothermal Au mineralization is significantly higher than in barren

256   felsic intrusions (Fig. 6), based on statistics of ~320 amphibole compositions

257   documented in the literature (Appendix Table 3).

258   Magnesio-ferri-hornblende in fertilized felsic intrusions accounts for ~70% of

259   the amphiboles analysed, and is followed by magnesio-hastingsite (22%) and small

260   amounts of actinolite, Ti-rich magnesio-hastingsite, and pargasite (Fig. 6a). In barren

261   intrusions, the proportion of magnesio-ferri-hornblende decreases significantly to

262   ~24%, whereas the proportion of magnesio-hastingsite increases to ~47%. Hastingsite

263   and ferro-ferri-hornblende occur only in barren intrusions and account for 20% and

264   8.6% of the amphibole population, respectively (Fig. 6b). Such difference and

265   variation in types and proportions of amphibole essentially reflect the change in

266   physical-chemical conditions and the compositional evolution of magmatic systems.

267   According to the thermobarometric formulations retrieved by Ridolfi et al. (2010), we

268   calculated crystallization physical-chemical parameters including pressure (P),

269   temperature (T), oxygen fugacity (f_{O2}), and H_2O_{melt} based on amphibole compositions

270   (Fig. 7). In the P-T diagram (Fig. 7a), magnesio-hastingsite and hastingsite

271   crystallized at relatively high temperatures (>800°C) and pressures (from 110 to 520

272   MPa), whereas magnesio-ferri-hornblende and actinolite formed under relatively low

273   temperatures and pressures. Oxygen fugacity calculated for amphiboles from barren

274   intrusions (FMQ to NNO+1) is generally lower by 1-2 orders of magnitude than that

275   calculated for amphiboles from fertilized intrusions (typically from NNO+1 to

276   NNO+3) (Fig. 7b). Figure 7c shows that H_2O_{melt} is indistinguishable between

277   amphiboles from fertilized and barren intrusions. Therefore, barren intrusions

278   characterized by dominant magnesio-hastingsite and distinctive hastingsite are

279   inferred to have crystallized in high P-T and low f_{O2} environments, while fertilized

280   intrusions characterized by predominant magnesio-ferri-hornblende with subordinate

281   magnesio-hastingsite and actinolite have formed under relatively low P-T but high f_{O2}

282   conditions.

283   A broad consensus is that porphyry-skarn polymetallic deposits are closely

284   associated with hydrous and oxidized magmas (e.g., Ballard et al., 2002; Richards,

285   2003; Sillitoe, 2010; An et al., 2015; Lu et al., 2016). In magmatic systems with a

286   high oxidation state (ΔFMQ>1.5–2), sulfur is dominantly present as sulfate, with the

287   result that chalcophile elements such as Cu and Au behave as incompatible elements

288   and are retained in the melt, which is conducive to the polymetallic mineralization in

289   the upper crust (e.g., Carroll and Rutherford, 1985; Richards, 2003; Mustard et al.,

290   2006; Sun et al., 2015; Duan and Jiang, 2017). Possible explanations for the high

291   oxidation state include the transfer of fluids and the effect of later crustal processes

292   including protracted fractionation and degassing of volatile-rich magmas (Lee et al.,

293   2010; Humphreys et al. 2015). Water, as the most abundant volatile in magmas, is

294   considered the key factor driving melt oxidation during degassing, however, recent

295   studies suggest that water degassing has no effect on oxidation (Crabtree and Lange,

296   2012; Waters and Lange, 2016). Given that f_{O2} of fertilized intrusions is significantly

297   higher than barren intrusions, while H_2O content of the two intrusion types is

298   basically overlapped as shown in this study (Fig. 7c), H_2O degassing might have little

299   effect on the oxidation state of magmatic liquids.

300   Recent study by Zhang et al. (2022) shows that bulk $Fe^{3+}/\Sigma Fe$ ratio of cumulates

301   from the Kohistan arc decreases from 0.4 to 0.2 with decreasing Mg#, as $Fe^{3+}/\Sigma Fe$

14

302   ratios in amphibole decrease from 0.35 to 0.2, leading to increasing Fe^{3+} abundance in

303   residual melts by multistage amphibole fractionation. Their modeling suggests that

304   amphibole fractionation could elevate the oxidation state of evolved magmas in

305   subduction zones, which is probably a reliable mechanism for triggering porphyry

306   copper mineralization in subduction settings. In our study, the $Fe^{3+}/\Sigma Fe$ ratios in

307   amphibole of barren intrusions are mostly less than 0.3 (from 0.21 to 0.32, Fig. 8a),

308   while the $Fe^{3+}/\Sigma Fe$ ratios in amphibole of fertilized intrusions have a wide range and

309   relatively high values (from 0.18 to 0.55). In terms of element occupation of

310   amphibole, both Fe^{2+} and Fe^{3+} at C site generally decrease from barren intrusions to

311   fertilized intrusions, with increasing of Mg at C site (Fig. 8b-c). Figure 8d shows a

312   positive liner correlation between Mg# and ΔNNO values, which is consistent with

313   other previous studies (Anderson and Smith, 1995; Scaillet and Evans, 1999; Ridolfi

314   et al., 2010; Shane and Smith, 2013), suggesting that Mg# values are redox-sensitive

315   and can be used to evaluate the oxidation state and fertility of porphyry magmas.

316   In summary, magnesio-ferri-hornblende that occurs as a dominant amphibole

317   species with relatively high Mg# values in mineralized intrusions is indicative of a

318   high fO₂ crystallization condition of its parent magma. Given that the more oxidized

319   felsic magma has a better sulfur-carrying capacity and is favorable for porphyry-skarn

320   mineralization, the extensive occurrence of magnesio-ferri-hornblende could be used

321   as a potential indicator for identifying fertile porphyry systems.

322   **Linkage between magma mixing and porphyry system mineralization**

323   Mafic magmatic enclaves (MMEs) occur commonly in felsic intrusions. The

15

324   mixing/mingling process between injected mafic magma and crustal magma is

325   considered to be the most likely formation mechanism (e.g., Barbarin, 2005; Kumar

326   and Rino, 2006; Chen et al., 2009; Clemens and Stevens, 2012; Cao et al., 2022). For

327   the felsic intrusions containing MMEs without mineralization clue at present, the

328   proportion of amphiboles (n=183) is similar to fertilized intrusions, but significantly

329   different from barren intrusions (Fig. 6). Amphiboles in the felsic intrusions with

330   magma mixing are predominated by magnesio-ferri-hornblende with a proportion of

331   86.7%, followed by actinolite (7.2%), magnesio-hastingsite (3.9%), magnesio-

332   hornblende (1.7%), and pargasite (0.6%). The occurrence of pargasite that represents

333   high-P mantle amphiboles (Ridolfi et al., 2010) in both felsic intrusions of magma

334   mixing origin and fertilized intrusions indicates a contribution of mantle-derived

335   magmas. In contrast, hastingsite and ferro-ferri-hornblende with low Mg# values

336   (<0.5) occur only in barren intrusions, indicating characteristics of crustal amphiboles

337   (Ridolfi et al., 2010). Significantly, MMEs were also observed in about half of

338   statistical fertilized intrusions (e.g., Kekeshala-Aimsduyi and Halegati-Muzuke skarn

339   type Fe-Cu deposits, Xilicuduke, Baogutu, Machagnqing, Jono and Pulang porphyry

340   Cu-Au-Mo deposits, Appendix Table 3 and references therein). The predominance of

341   the new mineral magnesio-ferri-hornblende in both fertilized magmas and unfertilized

342   magma mixing intrusions suggests that the recharge of mafic magma marked by

343   MMEs should play an important role in porphyry system mineralization.

344   Keith et al. (1997) proposed that the volcanic rocks from the Bingham and Tintic

345   districts (Utah) were formed by mixing of an S-rich mafic alkaline magmas with more

346   silicic magmas, indicating a large budget of mantle-derived S, Cu, Ag, and Au was

347   contributed to the process of the formation of porphyry and mesothermal vein world-

348   class deposits. Richards (2003) suggested that mixing between crustal- and mantle-

349   derived magmas yields evolved (andesitic to dacitic), volatile-rich, metalliferous,

350   hybrid magmas, which are of sufficiently low density to rise through the crust.

351   Mungall et al. (2015) used laboratory experiments to show that droplets of sulfide

352   melt in mafic magmas (which subsequently mix with more felsic magmas) can attach

353   to vapor bubbles to form compound drops that float, which is a key step in the

354   formation of porphyry deposits. Cao et al. (2022) identified two groups of amphibole

355   crystals with different mineral chemistry and suggested that MMEs and host granites

356   at the giant Pulang porphyry Cu-Au deposit in Tibet are sourced from mafic and felsic

357   magma reservoirs, respectively. Together with partitioning models, they proposed that

358   repeated mafic magma recharge may have supplied significant amounts of S and some

359   Cl, thus aiding formation of the large, long-lived magma reservoir that produced the

360   porphyry deposits. Indeed, recharge of mafic magma may contribute significant

361   amount of sulfur-, metal-, and/or chlorine-rich magmatic fluids to the felsic magma

362   (Hattori and Keith, 2001; Audétat and Simon, 2012; Zhang et al., 2019; Yang et al.,

363   2020; Cao et al., 2022) or remobilize precipitated magmatic sulfides (Wilkinson,

364   2013). Consequently, magma mixing recorded by MMEs and/or contemporaneous

365   mafic intrusions as well as massive magnesio-ferri-hornblende could be used to

366   identify felsic magma fertility that is particularly predisposed to ore formation.

367   However, not all felsic melts mixed with mafic magmas can eventually evolve into

368 fertile magmas required to generate ore deposits, because formation of porphyry ore

369 systems is controlled by the interplay of several processes, including cyclical

370 enrichment of magmas with metals and volatiles in the deep crust, sulfide saturation

371 of the magmas, efficient transfer of metals into hydrothermal fluids exsolved from the

372 magmas, and efficient precipitation of ore minerals at the deposit trap sites (Wilkinson,

373 2013).

374   **IMPLICATIONS**

375   Magnesio-ferri-hornblende, the new mineral found in felsic magmas, is ubiquitous

376 in both fertilized magmas related to porphyry ore system and granitoids containing

377 MMEs of magma mixing origin, but rare in barren intrusions. Our findings indicate

378 that amphibole compositions and proportions, especially massive occurrences of

379 magnesio-ferri-hornblende in felsic magmas may represent a potential application as a

380 useful tool to identify ore-bearing and barren intrusions within porphyry-skarn and

381 hydrothermal polymetallic deposits. Amphiboles in barren intrusions are dominantly

382 characterized by magnesio-hastingsite and hastingsite crystallized in high P-T and low

383 f_{O2} environments. The distinctive hastingsite and ferro-ferri-hornblende observed only

384 in barren intrusions are mainly crustal amphiboles (high Fe^{2+} at C sites and Mg#<0.5).

385 Felsic magmas with ore-potential record evidence of lower P-T and high f_{O2}

386 conditions, characterized by predominant magnesio-ferri-hornblende and subordinate

387 magnesio-hastingsite that have low Fe^{2+} at C site and high Mg# values. Importantly,

388 amphibole compositions could be an effective exploration indicator, based on an

389 empirical relationship between magmatic f_{O2} and Mg# (Ridolfi et al., 2010). Magma

390   mixing process has been genetically linked to porphyry system mineralization.

391   However, there are also felsic rocks containing MMEs that have not shown clues of

392   mineralization yet, which should be paid attention in the further target mineralization

393   exploration.

411   REFERENCES CITED

412   An, F., Wang, J.L., Zhu, Y.F., Wang, J.Q., Wei, S.N., Lai, S.C., and Eleonora, S. (2015)

413   Mineralogy and geochemistry of intrusions related to Sayak large copper deposit,

414   Kazakhstan, Central Asian metallogenic belt: Magma nature and its significance

415   to mineralization. Acta Petrologica Sinica, 31, 555–570 (In Chinese with English

416   abstract).

417   Anderson, J.L., and Smith, D.R. (1995) The effects of temperature and fO_2 on the Al-

418   in-hornblende barometer. American Mineralogist, 80, 549–559.

419   Apopei, A.I. and Buzgar, N. (2010) The Raman study of amphiboles. Universitatea Al.

420   I. Cuza Din Iasi. Analele Stiintifice. Geologie, 56, 57–83.

421   Audétat, A., and Simon, A.C. (2012) Magmatic controls on porphyry Cu genesis. In

422   J.W. Hedenquist, M. Harris, and F. Camus, Eds., Geology and genesis of major

423   copper deposits and districts of the world: A tribute to Richard Sillitoe. Society

424   of Economic Geologists, Special Publication, 16, 553–572.

425   Ballard, J.R., Palin, M.J., and Campbell, I.H. (2002) Relative oxidation states of

426   magmas inferred from Ce(IV)/Ce(III) in zircon: application to porphyry copper

427   deposits of northern Chile. Contributions to Mineralogy and Petrology, 144,

428   347–364.

429   Barbarin, B. (2005) Mafic magmatic enclaves and mafic rocks associated with some

430   granitoids of the central Sierra Nevada batholith, California: Nature, origin, and

431   relations with the hosts. Lithos, 80, 155–177.

432   Cao, K., Yang, Z.M., White, N.C., and Hou, Z.Q. (2022) Generation of the giant

433   porphyry Cu-Au deposit by repeated recharge of mafic magmas at Pulang in

434   Eastern Tibet. Economic Geology, 117, 57–90.

435   Carroll, M.R., and Rutherford, M.J. (1985) Sulfide and sulfate saturation in hydrous

436   silicate melts. Journal Geophysical Research, 90, C601–C612.

437   Chen, B., Chen, Z.C., and Jahn, B.M. (2009) Origin of mafic enclaves from the

438   Taihang Mesozoic orogen, north China craton. Lithos, 110, 343–358.

439   Chukanov, N.V., and Chervonnyi, A.D. (2016) IR spectra of minerals and related

440   compounds, and reference samples' data. Infrared Spectroscopy of Minerals and

441   Related Compounds, 51–1047.

442   Clemens, J.D., and Stevens, G. (2012) What controls chemical variation in granitic

443   magmas? Lithos, 134-135, 317–329.

444   Crabtree, S.M., and Lange, R.A. (2012) An evaluation of the effect of degassing on

445   the oxidation state of hydrous andesite and dacite magmas: a comparison of pre-

446   and post-eruptive Fe^{2+} concentrations. Contributions to Mineralogy and

447   Petrology, 163, 209–224.

448   Duan, D.F., and Jiang, S.Y. (2017) In situ major and trace element analysis of

449   amphiboles in quartz monzodiorite porphyry from the Tonglvshan Cu–Fe (Au)

450   deposit, Hubei Province, China: insights into magma evolution and related

451   mineralization. Contributions to Mineralogy and Petrology 172, 1-17.

452   El-Shazly, A.K., Worthing, M.A., and Liou, J.G. (1997) Interlayered eclogites,

453   blueschists and epidote amphibolites from NE Oman: a record of protolith

454   compositional control and limited fluid infiltration. Journal of Petrology, 38, 1461–

455   1487.

456   Ghent, E.D., Stout, M.Z., and Erdmer, P. (1990) Howieite in blueschists, Pinchi Lake,

457   British Columbia. The Canadian Mineralogist, 28, 855–858.

458   Gil, G., Borowski, M.P., Barnes, J.D., Jokubauskas, P., Bagiński, B., Gunia, P., and

459   Ilnicki, S. (2022) Formation of serpentinite-hosted talc in a continental crust setting:

460   Petrographic, mineralogical, geochemical, and O, H and Cl isotope study of the

461   Gilów deposit, Góry Sowie Massif (SW Poland). Ore Geology Reviews, 146,

462   104926.

463   Gong, L., Chen, H.Y., Xiao, B., Wang, Y.F., and Zhao, L.D. (2018) Mineral chemistry

464   of hornblende in the Chihu-Fuxing copper district, Xinjiang, and its geological

465   significance. Geochimica, 47, 149–168 (In Chinese with English abstract).

466   Gu, X.X., Zhang, Y.M., Peng, Y.W., Zhang, L.Q., Wang, X.L., Gao, H., Dong, L.H.,

467   and Tu, Q.J. (2014) The Fe-Cu-Mo polymetallic mineralization system related to

468   intermediateacid intrusions in the Boluokenu metallogenic belt of the West

469   Tianshan, Xinjiang: Rock-and ore-forming geochemistry and tectonomagmatic

470   evolution. Earth Science Frontiers, 21, 156–175 (In Chinese with English

471   abstract).

472   Hammarstrom, J.M., and Zen, E.A. (1986) Aluminum in hornblende: an empirical

473   igneous geobarometer. American Mineralogist, 71, 1297–1313.

474   Hatert, F., and Burke, E.A.J. (2010) The IMA-CNMNC dominant-constituent rule

475   revisited and extended. Elements, 6, 24.

476   Hattori, K.H., and Keith, J.D. (2001) Contribution of mafic melt to porphyry copper

477   mineralization: Evidence from Mount Pinatubo, Philippines, and Bingham

478   Canyon, Utah, USA. Mineralium Deposita, 36, 799–806.

479   Hawthorne, F.C., Oberti, R., Harlow, G.E., Maresch, W.V., Martin, R.F., Schumacher,

480   J.C., and Welch, M.D. (2012) Nomenclature of the amphibole supergroup.

481   American Mineralogist, 97, 2031–2048.

482   Hawthorne, F.C., Oberti, R., Ventura, G.D., and Mottana, A. (2007) Amphiboles:

483   Crystal   chemistry, occurrence and health issues.   Reviews   in   Mineralogy   and

484   Geochemistry, 67, 545.

485   Hawthorne, F.C., Ungaretti, L., and Oberti, R. (1995) Site populations in minerals:

486   terminology   and   presentation   of   results   of   crystal-structure   refinement.   The

487   Canadian Mineralogist, 33, 907–911.

488   He, Y., Zhang, Y.M., Gu, X.X., Peng, Y.W., Cheng, W.B., Wang, G.N., Wan, Y., and

489   Yuan, P. (2018) Mineral chemistry of Husite pluton in West Tianshan, Xinjiang

490   and its implications for petrogenesis and mineralization. Geoscience, 32, 1227–

491   1241 (In Chinese with English abstract).

492   Horváth, L., Gault, R.A., Pfenninger-Horváth, E., and Poirier, G. (2020) Mont Saint-

493   Hilaire: history,   geology,   mineralogy.   The   Canadian   Mineralogist,   Special

494   Publications, 58, 543-545.

495   Huang, E.P. (2003) Raman Spectroscopic Study of Amphiboles. PhD thesis, Southern

496   Medical University, Guangzhou, China (In Chinese with English abstract).

497   Humphreys, M.C.S., Brooker, R.A., Fraser, D.G., Burgisser, A., Mangan, M.T., and

498   McCammon, C. (2015) Coupled interactions between volatile activity and Fe

499   oxidation state during arc crustal processes. Journal of Petrology, 56, 795–814.

500   Keith, J.D., Whitney, J.A., Hattori, K., Ballantyne, G.H., Christiansen, E.H., Barr,

501   D.L., Cannan, T.M., and Hook, C.J. (1997) The role of magmatic sulfides and

502   mafic alkaline magmas in the Bingham and Tintic mining districts, Utah. Journal

503   of Petrology, 38, 1679–1690.

504   Kloprogge, J. T., Visser, D., Ruan, H., Frost, R.L. (2001) Infrared and Raman

505   spectroscopy of holmquistite, $Li_2(Mg,Fe^{2+})_3(Al,Fe^{3+})_2(Si,Al)_8O_{22}(OH)_2$. Journal

506   of Materials Science Letters, 20, 1497-1499.

507   Kumar, S., and Rino, V. (2006) Mineralogy and geochemistry of microgranular

508   enclaves in Palaeoproterozoic Malanjkhand granitoids, central India: evidence of

509   magma mixing, mingling, and chemical equilibration. Contributions to

510   Mineralogy and Petrology, 152, 591–609.

511   Leake, B.E., Woolley, A.R., Arps, C.E.S., Birch, W.D., Gilbert, M.C., Grice, J.D.,

512   Hawthorne, F.C., Kaato, A., Kisch, H.J., and Krivovichev, V.G. (1997)

513   Nomenclature of amphibole: Report of the subcommittee on amphiboles of the

514   International Mineralogical Association, Commission on New Minerals and

515   Mineral Names. American Mineralogist, 82, 1019–1037.

516   Lee, C.T.A., Luffi, P., Roux, V.L., Dasgupta, R., Albaréde, F., and Leeman, W.P. (2010)

517   The redox state of arc mantle using Zn/Fe systematics. Nature, 468, 681–685.

518   Liu, X., Qian, Q., Su, W., and Li, J.L. (2012) Pluton from Muhanbasitao in the

519   western of Awulale, Western Tianshan: Geochemistry, geochronology and

520   geological implications. Acta Petrologica Sinica, 28, 2401–2413 (In Chinese

521   with English abstract).

522   Long, L.L., Gao, J., Klemd, R., Beier, C., Qian, Q., Zhang, X., Wang, J.B., and Jiang,

523   T. (2011) Geochemical and geochronological studies of grantioid rocks from the

524   Western Tianshan Orogen: Implications for continental growth in the southwestern

525   Central Asian Orogenic Belt. Lithos, 126, 321–340.

526   Lu, Y.J., Loucks, R.R., Fiorentini, M., McCuaing, T.C., Evans, N.J., Yang, Z.M., Hou,

527   Z.Q., Kirkland, C.L., Parra-Avila, L.A., and Kobussen, A. (2016) Zircon

528   compositions as a pathfinder for porphyry Cu ± Mo ± Au deposits. Society

529   Economic Geologists, Special Publications, 19, 329–347.

530   Mandarino, J. A. (1981) The Gladstone-dale relationship: part IV, The compatibility

531   concept and its application. The Canadian Mineralogist, 19, 441–445.

532   Mogessie, A., Hauzenberger, C.A., Hoinkes, G., Felfernig, A., Stumpfl, E.F., Bjerg,

533   E.A., and Kostadinoff, J. (2000) Genesis of platinum-group minerals in the Las

534   Aguilas mafic-ultramafic rocks, San Luis Province, Argentina: textural, chemical

535   and mineralogical evidence. Mineralogy and Petrology, 68, 85–114.

536   Mungall, J.E., Brenan, J.M., Godel, B., Barnes, S.J., and Gaillard, F. (2015) Transport

537   of metals and sulphur in magmas by flotation of sulphide melt on vapour bubbles.

538   Nature Geoscience 8, 216–219.

539   Mustard, R., Ulrich, T., Kamenetsky, V.S., and Mernagh, T. (2006) Gold and metal

540   enrichment in natural granitic melts during fractional crystallization. Geology, 34,

541   85–88.

542   Mutch, E.J.F., Blundy, J.D., Tattitch, B.C., Cooper, F.J., and Brooker, R.A. (2016) An

543   experimental study of amphibole stability in low-pressure granitic magmas and a

544   revised Al-in-hornblende geobarometer. Contributions to Mineralogy and

545   Petrology, 171, 85.

546   Nickel, V.E.H., and Grice, C.J.D. (1998) The IMA commission on new minerals and

547   mineral names: procedures and guidelines on mineral nomenclature, 1998.

548   Mineralogy and Petrology, 64, 237–263.

549   Oberti, R., Boiocchi, M., Hawthorne, F.C., Ball, N.A., and Chiappino, L. (2016a)

550   Magnesio-ferri-fluoro-hornblende from Portoscuso, Sardinia, Italy: description

551   of a newly approved member of the amphibole supergroup. Mineralogical

552   Magazine, 80, 269–275.

553   Oberti, R., Boiocchi, M., Hawthorne, F.C., Ball, N.A., Cámara, F., Pagano, R., and

554   Pagano, A. (2016b) Ferro-ferri-hornblende from the Traversella Mine (Ivrea,

555   Italy): occurrence, mineral description and crystal-chemistry. Mineralogical

556   Magazine, 80, 1233–1242.

557   Oberti, R., Hawthorne, F.C., Cannillo, E., and Cámara, F. (2007) Long-range order in

558   amphiboles. Reviews in Mineralogy and Geochemistry, 67, 125–172.

559   Oberti, R., Boiocchi, M., Hawthorne, F.C., and Ciriotti, M.E. (2018) Magnesio-

560   hornblende from Lüderitz (Namibia): mineral description and crystal chemistry.

561   Mineralogical Magazine, 82: 1253–1259.

562   O'Neill, H.S.C. (1987a) Quartz-fayalite-iron and quartz-fayalite-magnetite equilibria

563   and the free energy of formation of fayalite (Fe_2SiO_4) and magnetite (Fe_3O_4).

564   American Mineralogist, 72, 67–75.

565   O'Neill, H.S.C. (1987b) Free energies of formation of NiO, CoO, Ni_2SiO_4, and

566   Co_2SiO_4. American Mineralogist, 72, 280–291.

567   Richards, J.P. (2003) Tectono-magmatic precursors for porphyry Cu-(Mo-Au) deposit

568   formation. Economic Geology, 98, 1515–1533.

569   Ridolfi, F., and Renzulli, A. (2012) Calcic amphiboles in calc-alkaline and alkaline

570   magmas: thermobarometric and chemometric empirical equations valid up to

571   1,130 °C and 2.2 GPa. Contributions to Mineralogy and Petrology, 163, 877–895.

572   Ridolfi, F., Renzulli, A., and Puerini, M. (2010) Stability and chemical equilibrium of

573   amphibole in calc-alkaline magmas: an overview, new thermobarometric

574   formulations and application to subduction-related volcanoes. Contributions to

575   Mineralogy and Petrology, 160, 45–66.

576   Rinaudo, C., Belluso, E., Gastaldi, D. (2004) Assessment of the use of Raman

577   spectroscopy for the determination of amphibole asbestos. Mineralogical

578   Magazine, 68, 443-453.

579   Scaillet, B., and Evans, B.W. (1999) The 15 June 1991 Eruption of Mount Pinatubo. I.

580   Phase equilibria and pre-eruption P-T-fO_2-fH_2O conditions of the dacite magma.

581   Journal of Petrology, 40, 381–411.

582   Schwab, R.G., and Kuestner, D. (1981) The equilibrium fugacities of important

583   oxygen buffers in technology and petrology. Neues Jahrb. Mineral., Abh., 140,

584   111–142.

585   Shane, P., and Smith, V.C. (2013) Using amphibole crystals to reconstruct magma

586   storage temperatures and pressures for the post-caldera collapse volcanism at

27

587   Okataina volcano. Lithos, 156, 159-170.

588 Sillitoe, R.H. (2010) Porphyry copper systems. Economic Geology, 105, 3–41.

589 Stepanov, S.Y., Palamarchuk, R.S., Varlamov, D.A., Kiseleva, D.V., Sharpyonok, L.N.,

590   Škoda, R., and Kasatkin, A.V. (2021) The features of native gold in ore-bearing

591   breccias with realgar-orpiment cement of the vorontsovskoe deposit (Northern

592   Urals, Russia). Minerals, 11, 541.

593 Su, W., Zhang, M., Redfern, S.A.T., Gao, J., and Klemd, R. (2009) OH in zoned

594   amphiboles of eclogite from the western Tianshan, NW-China. International

595   Journal of Earth Sciences, 98, 1299–1309.

596 Sun, W., Huang, R.F., Li, H., Hu, Y.B., Zhang, C.C., Sun, S.J., Zhang, L.P., Ding, X.,

597   Li, C.Y., Zartman, R.E., and Ling, M.X. (2015) Porphyry deposits and oxidized

598   magmas. Ore Geology Reviews, 65, 97–131.

599 Wang, G.N., Zhang, Y.M., Gu, X.X., Peng, Y.W., and He, Y. (2018) Petrogenesis and

600   mineralization of the porphyry and skarn mineralization-related Husite intrusion

601   in the Boluokenu metallogenic belt, Western Tianshan Orogenic Belt, NW China.

602   Journal of Asian Earth Sciences, 165, 160–174.

603 Waters, L.E., and Lange, R.A. (2016) No effect of H_2O degassing on the oxidation

604   state of magmatic liquids. Earth and Planetary Science Letters, 447, 48–59.

605 Wilkinson, J.J. (2013) Triggers for the formation of porphyry ore deposits in

606   magmatic arcs. Nature Geoscience, 6, 917–925.

607 Yang, M.M., Zhao, F.F., Liu, X.F., Qing, H.R., Chi, G.X., Li, X.Y., Duan, W.J., and

608   Lai, C.K. (2020) Contribution of magma mixing to the formation of porphyry-

609   skarn mineralization in a post-collisional setting: The Machangqing Cu-Mo-(Au)

610   deposit, Sanjiang tectonic belt, SW China. Ore Geology Reviews, 122, 103518.

611 Zarubina, E.S., Aksenov, S.M., Chukanov, N.V., and Rastsvetaeva, R.K. (2016)

612   Crystal structure of magnesio-ferri-hornblendite

613      $\square Ca_2(Mg_4Fe^{3+})[(Si_7Al)O_{22}](OH)_2$ as a potentially new mineral of the amphibole

614   supergroup. Doklady Chemistry, 470, 245–251.

615 Zhang, J., Wang, R., and Hong, J. (2022) Amphibole fractionation and its potential

616   redox effect on arc crust: Evidence from the Kohistan arc cumulates. American

617   Mineralogist, 107, 1779–1788.

618 Zhang, X.W., Cheng, Y.H., Li, Y.J., Xu, X., Teng, X.J. Wang, S.Y., Li, Y., and Liu,

619   H.D. (2021) Zircon U-Pb dating and geochemistry of the Late Carboniferous

620   hornblendite in Dong Ujimqi Inner Mongolia and its tectonic significance. Acta

621   Geologica Sinica, 95, 1495–1507 (In Chinese with English abstract).

622 Zhang, Y., Gu, X., Li, T., Fan, G., Zhang, Y., and Wang, J. (2022) Magnesio-ferri-

623   hornblende, IMA 2021-100, in: CNMNC Newsletter 66. European Journal of

624   Mineralogy, 34, 253-257.

625 Zhang, Y.M., Zhang, L.Q., Gao, H., Li, W.D., Hu, Z.J., Wan, Y., and Yuan, P. (2016)

626   Petrology, zircon U-Pb geochronology and Hf isotopes of the Husite complex in

627   West Tianshan, Xinjiang. Acta Petrologica Sinica, 32, 1749–1769 (In Chinese

628   with English abstract).

629 Zhang, Z.B., Tang, J.X., Tang, P., Chen, G.L., Zhang, Z.K., Gao, X., and Yang, Y.

630   (2019) The origin of the mafic microgranular enclaves from Jiama porphyry Cu

29

631   polymetallic deposit, Tibet: Implications for magma mixing/mingling and

632   mineralization. Acta Petrologica Sinica, 35, 934–952 (In Chinese with English

633   abstract).

634   **FIGURE CAPTIONS**

635   **FIGURE 1.** (a) Sketch tectonic map of the Central Asian Orogenic Belt (modified

636   after Long et al., 2011); (b) Geological map of the Western Tianshan (NW

637   China), showing the location of major skarn and porphyry deposits (modified

638   after Wang et al., 2018, and references therein); (c) Regional geologic map of the

639   Boluokenu area in the Western Tianshan (modified after Gu et al., 2014 and

640   Zhang et al., 2016). Magnesio-ferri-hornblende was found in the granitoids

641   marked by yellow stars.

642   **FIGURE 2.** Photographs showing occurrence of magnesio-ferri-hornblende. (a) Hand

643   specimen photo of granodiorite from the Husite complex that contains magnesio-

644   ferri-hornblende. (b) Thin section of granodiorite containing magnesio-ferri-

645   hornblende (mosaics of multiple images taken in plane-polarized light). (c and d)

646   Magnesio-ferri-hornblende is associated with plagioclase, quartz, K-feldspar, and

647   biotite (viewed in plane-polarized light). Mfhbl = magnesio-ferri-hornblende; Pl

648   = plagioclase; Qtz = quartz; Kf = K-feldspar; Bt = biotite.

649   **FIGURE 3.** The Mössbauer spectrum of magnesio-ferri-hornblende

650   **FIGURE 4.** The infrared spectrum of magnesio-ferri-hornblende

651   **FIGURE 5.** The Raman spectrum of magnesio-ferri-hornblende

652   **FIGURE 6.** Pie graphs showing proportion of amphiboles under different geological

653   backgrounds. (a) Amphiboles in felsic magmas related to porphyry-skarn Fe-Cu-

654   Mo-Au and hydrothermal Au mineralization; (b) Amphiboles from barren felsic

655   magmas in the same ore belt of fertilized magmas; (c) Amphiboles in felsic

656   magmas containing mafic magmatic enclaves (MMEs) of magma mixing origin,

657   where no mineralization clue has yet been found.

658   **FIGURE 7.** P–T (a), logf_{O2}–T (b), and T–H_2O_{melt} (c) diagrams for several types of

659   amphiboles from fertile and barren felsic intrusions. The curves FMQ, NNO and

660   MH are after O'Neill (1987a, 1987b) and Schwab and Küstner (1981). Owing to

661   the applicability of amphibole thermobarometry (Ridolfi et al., 2010), T-P-

662   H_2O_{melt}-f_{O2} parameters were partially determined for certain amphiboles. Mfhbl =

663   Magnesio-ferri-hornblende, Mhst = Magnesio-hastingsite, Ti-Mhst = Ti-rich

664   Magnesio-hastingsite, Act = Actinolite, Hst = Hastingsite.

665   **FIGURE 8.** (a) Fe^{3+}/ΣFe ratios versus Mg# diagram for amphiboles; (b and c) $^CFe^{2+}$

666   and $^CFe^{3+}$ versus ^CMg diagrams for amphiboles; (d) ΔNNO values versus Mg#

667   diagram for amphiboles. Mg# = atomic [Mg/(Mg+Fe$_T$)], where Fe$_T$ = Fe^{2+} + Fe^{3+}.

668   Mfhbl = Magnesio-ferri-hornblende, Mhst = Magnesio-hastingsite, Ti-Mhst = Ti-

669   rich Magnesio-hastingsite, Act = Actinolite, Prg = Pargasite, Hst = Hastingsite,

670   Ffhbl = Ferro-ferri-hornblende.

671   **TABLE CAPTIONS**

672   **TABLE 1.** ^{57}Fe hyperfine parameters for magnesio-ferri-hornblende

673   **TABLE 2.** Chemical composition (wt%) and unit formula (apfu) for magnesio-ferri-

674   hornblende

31

675 **TABLE 3.** X-ray powder diffraction data (*d* in Å) for magnesio-ferri-hornblende

676 **TABLE 4.** Selected interatomic distances (Å) for magnesio-ferri-hornblende

677 **TABLE 5.** Site populations (apfu) for magnesio-ferri-hornblende

678 **TABLE 6.** Predominant-constituents in the structural sites of magnesio-ferri-

679 hornblende in the hornblende species approved so far

680 **SUPPLEMENTAL MATERIALS**

681 **APPENDIX TABLE 1.** Miscellaneous information for magnesio-ferri-hornblende.

682 **APPENDIX TABLE 2.** Atomic coordinates, equivalent isotropic and anisotropic atomic

683 displacement parameters ($Å^2$) for magnesio-ferri-hornblende.

684 **APPENDIX TABLE 3.** Major elements (wt%) from electron microprobe analysis and

685 calculated physical-chemical conditions of amphiboles from felsic fertilized

686 intrusions (a), barren intrusions (b) and intrusions of magma mixing origin (c).

687 **ONLINE MATERIAL.** The Crystallographic Information File (CIF) for magnesio-ferri-

688 hornblende.

TABLE 1. ^{57}Fe hyperfine parameters for magnesio-ferri-hornblende

Component	Isomer shift(mm/s)	Quadrupole splitting (mm/s)	Line width (mm/s)	Area (%)
Fe^{2+}	0.964±0.003	2.431±0.007	0.571±0.011	77.62
Fe^{3+}	0.046±0.007	0.935±0.014	0.384±0.020	22.38

TABLE 2. Chemical composition (wt%) and unit formula (apfu) for

magnesio-ferri-hornblende

Constituent	Mean	Range	SD* (σ)		apfu
SiO_2	47.37	46.76-48.29	0.489	Si^{4+}	6.94
TiO_2	1.51	1.28-1.78	0.166	Al^{3+}	1.06
Al_2O_3	7.07	6.4-7.6	0.363	ΣT	8.00
FeO_{total}	15.09	13.78-16.07	0.700	Al^{3+}	0.16
Fe_2O_3**	3.86			Ti^{4+}	0.17
FeO**	11.62			Fe^{3+}	0.43
MgO	12.77	12.05-13.94	0.587	Fe^{2+}	1.42
CaO	11.22	10.66-11.55	0.217	Mg^{2+}	2.79
SrO	0.15	0.09-0.21	0.030	Mn^{2+}	0.05
MnO	0.39	0.26-0.48	0.062	Sr^{2+}	0.01
Na_2O	1.54	1.30-1.95	0.141	Ca^{2+}	1.76
K_2O	0.78	0.58-0.93	0.084	Na^+	0.21
Cl	0.15	0.06-0.20	0.030	$\Sigma B+C$	7.00
Cl≡O	-0.03			Na^+	0.23
H_2O^+★★	2.01			K^+	0.15
F	0			ΣA	0.38
Total	100.41			Cl^-	0.04
				$(OH)^-$	1.96
				ΣW	2.00

Note: **Conversion of FeO_{total} by Mössbauer spectrum data; ★★Stoichiometric calculation on the basis of structural refinement; SD* Standard deviation, quoted at 1σ level

TABLE 3. X-ray powder diffraction data (d in Å) for magnesio-ferri-hornblende

I_{meas}	d_{meas}	d_{calc}	h	k	l
52	**8.397**	**8.466**	**1**	**1**	**0**
7	5.082	5.115	1	3	0
26	4.890	4.906	1	$\bar{1}$	$\bar{1}$
21	4.526	4.538	0	4	0
3	4.222	4.233	2	2	0
26	3.882	3.898	1	$\bar{3}$	$\bar{1}$
41	**3.383**	**3.395**	**1**	**5**	**0**
27	3.279	3.293	2	4	0
38	3.134	3.142	3	1	0
22	2.947	2.957	1	$\bar{5}$	$\bar{1}$
6	2.803	2.822	3	3	0
100	**2.717**	**2.723**	**1**	**5**	**1**
84	**2.597**	**2.608**	**0**	**6**	**1**
61	**2.545**	**2.548**	**2**	**0**	**$\bar{2}$**
26	2.341	2.349	3	$\bar{5}$	$\bar{1}$
26	2.298	2.311	1	$\bar{7}$	$\bar{1}$
9	2.218	2.222	2	$\bar{4}$	$\bar{2}$
37	2.167	2.176	2	6	1
20	2.131	2.131	4	$\bar{4}$	$\bar{1}$
18	2.022	2.024	4	0	$\bar{2}$
49	**1.854**	**1.855**	**1**	**$\bar{7}$**	**$\bar{2}$**
5	1.813	1.811	1	9	1
2	1.750	1.754	5	$\bar{1}$	$\bar{2}$
33	1.691	1.691	3	$\bar{1}$	$\bar{3}$
16	1.653	1.653	4	$\bar{8}$	$\bar{1}$
21	1.623	1.626	1	11	0
39	1.585	1.585	5	$\bar{5}$	$\bar{2}$
62	**1.519**	**1.518**	**6**	**$\bar{2}$**	**$\bar{2}$**
14	1.476	1.475	3	7	2
12	1.460	1.460	1	$\bar{7}$	$\bar{3}$
28	1.341	1.340	3	9	2
37	1.299	1.297	0	14	0

Note: The intensities of the seven strongest lines are in **bold**.

TABLE 4. Selected interatomic distances (Å) for magnesio-ferri-hornblende

A(m)	-O5×2	2.9840	A(2)	-O5×2	2.6200
	-O6×2	2.8280		-O6×2	2.8300
	-O7	2.5710		-O7×2	2.5390
	-O7	2.4920		<A(2)-O>	2.6630
	<A(m)-O>	2.7812			
M(4)	-O2×2	2.4124	M(4')	-O2×2	2.1400
	-O4×2	2.3251		-O4×2	2.2740
	-O5×2	2.7210		-O5×2	2.9360
	-O6×2	2.5395		-O6×2	2.8090
	<M(4)-O>	2.4995		<M(4')-O	2.5398
M(1)	-O1×2	2.0610	M(2)	-O1×2	2.1112
	-O2×2	2.1192		-O2×2	2.0862
	-O3×2	2.0949		-O4×2	1.9933
	<M(1)-O>	2.0917		<M(2)-O>	2.0636
M(3)	-O1×4	2.0961	T(1)	-O1	1.6382
	-O3×2	2.0834		-O6	1.6604
	<M(3)-O>	2.0919		-O7	1.6398
T(2)	-O4	1.5990		-O5	1.6613
	-O5	1.6491		< T(1)-O>	1.6499
	-O2	1.6260			
	-O6	1.6630			
	<T(2)-O>	1.6343			

TABLE 5. Site populations (apfu) for magnesio-ferri-hornblende

Site	Site population(apfu)	Site scattering (epfu)		Bond distance (Å)	
		Refined	Calculated	Refined	Calculated
T(1)	2.94Si+1.06Al	54.94	54.94		
T(2)	4Si	56.00	56.00		
M(1)	1.3Mg+0.7Fe^{2+}	34.86	33.80	2.093	2.092
M(2)	0.94Mg+0.3Fe^{2+}+0.43Fe^{3+}+0.16Al+0.17Ti	34.16	36.08	2.063	2.064
M(3)	0.55Mg+0.42Fe^{2+}+0.03Mn	18.09	18.30	2.092	2.092
ΣC cations		87.12	88.18		
B cations	1.76Ca+0.21Na+0.02Mn+0.01Sr	39.72	38.39		
A cations	0.23Na+0.15K	6.03	5.38		
W cations	1.93OH+0.07Cl	19.84	18.56		

TABLE 6. Predominant-constituents in the structural sites of magnesio-ferri-hornblende

in the hornblende species approved so far

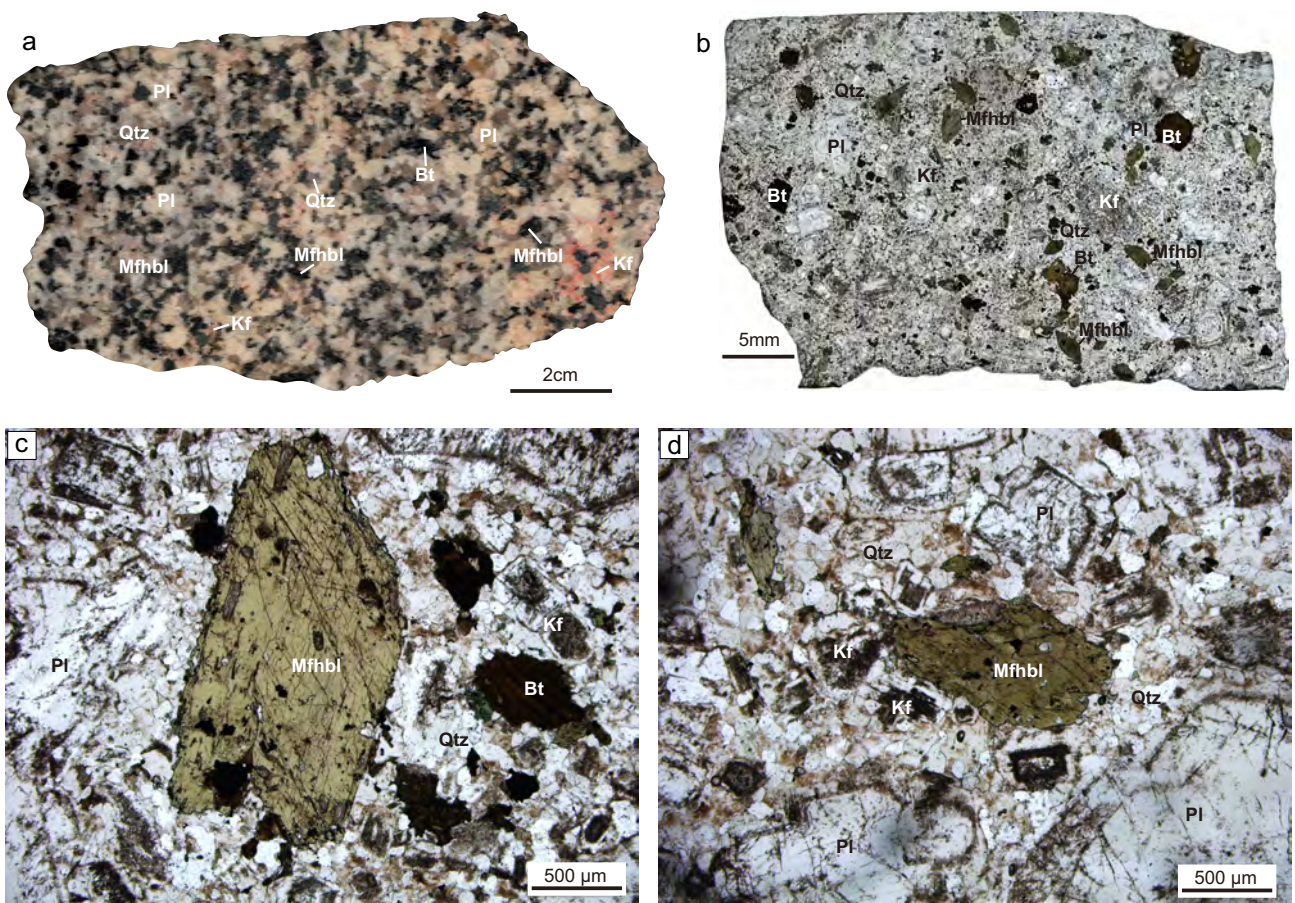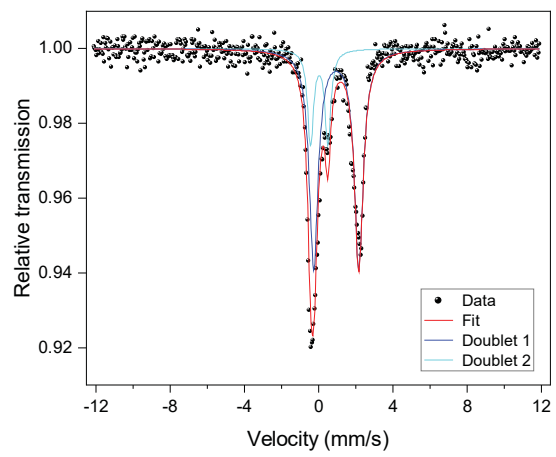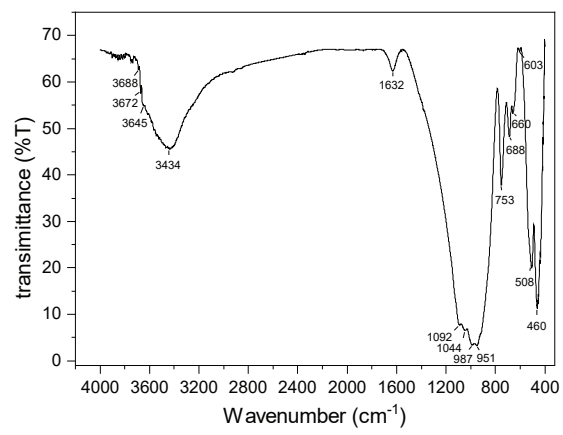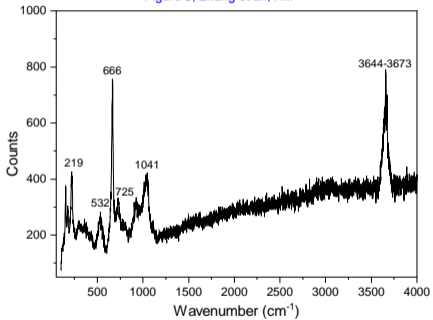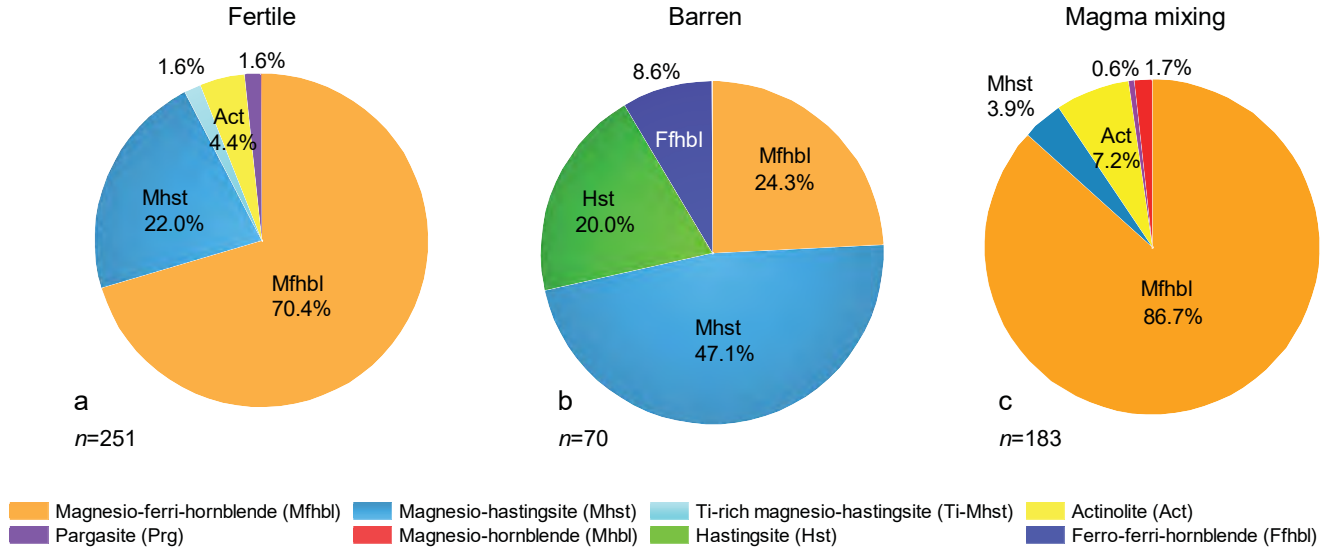| Mineral name	Site occupation						Reference
	A	B	C^{2+}	C^{3+}	T	W	
Magnesio-ferri-hornblende	□	Ca	Mg	Fe^{3+}	Si_7Al	OH	This work
Magnesio-hornblende	□	Ca	Mg	Al	Si_7Al	OH	Oberti et al. (2018)
Ferro-hornblende	□	Ca	Fe	Al	Si_7Al	OH	Hawthorne et al. (2012)
Magnesio-ferri-fluoro-hornblende	□	Ca	Mg	Fe^{3+}	Si_7Al	F	Oberti et al. (2016a)
Ferro-ferri-hornblende	□	Ca	Fe^{2+}	Fe^{3+}	Si_7Al	OH	Oberti et al. (2016b)

Figure 1, Zhang et al., *AM*
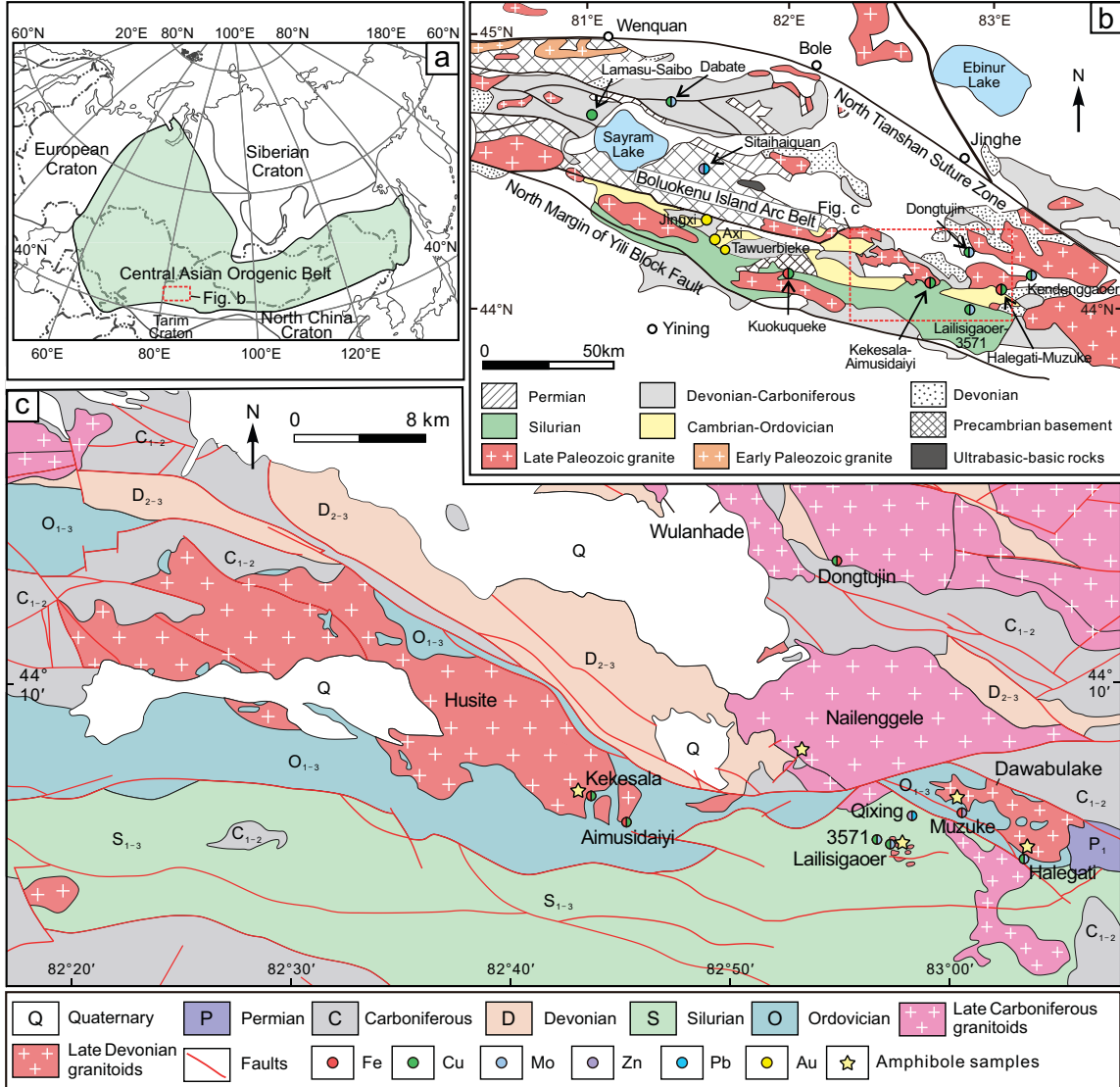
Figure 2, Zhang et al., *AM*

Figure 5, Zhang et al., *AM*

Figure 6, Zhang et al., *AM*

Fertile

1.6%
1.6%
Act
4.4%
Mhst
22.0%
Mfhbl
70.4%

a

n=251

Barren

8.6%
Ffhbl
Hst
20.0%
Mfhbl
24.3%
Mhst
47.1%

b

n=70

Magma mixing

Mhst
3.9%
0.6% 1.7%
Act
7.2%
Mfhbl
86.7%

c

n=183

- Magnesio-ferri-hornblende (Mfhbl)
- Pargasite (Prg)
- Magnesio-hastingsite (Mhst)
- Magnesio-hornblende (Mhbl)
- Ti-rich magnesio-hastingsite (Ti-Mhst)
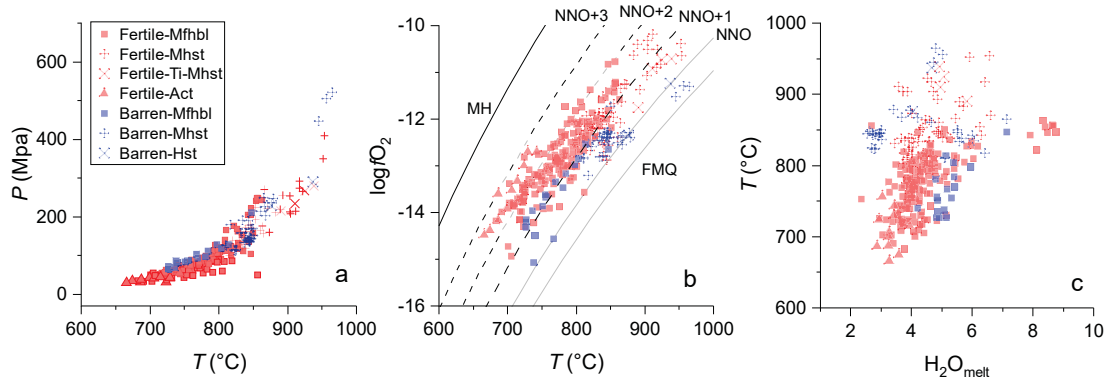- Hastingsite (Hst)
- Actinolite (Act)
- Ferro-ferri-hornblende (Ffhbl)

Figure 7, Zhang et al., *AM*